New Insights into the Molecular Structures, Compositions, and Cation Distributions in Synthetic and Natural Montmorillonite Clays

Sylvian Cadars,[1] Régis Guégan,[2,3] Mounesha N. Garaga,[1] Xavier Bourrat,[2,3] Lydie Le Forestier,[2,3] Franck Fayon,[1] Tan Vu Huynh,[1] Teddy Allier,[1] Zalfa Nour,[1] and Dominique Massiot[1]*

[1] CEMHTI CNRS UPR3079, université d'Orléans, 1D avenue de la recherche-scientifique, 45071 Orléans Cédex 2, France

[2] Université d'Orléans, ISTO, UMR 7327, 45071 Orléans, France

[3] CNRS/INSU, ISTO, UMR 7327, 45071 Orléans, France

***** to whom correspondence should be addressed. E-mail: sylvian.cadars@cnrs-orleans.fr

Supporting Information

Table S1. Description of pseudopotentials used for planewave-based DFT calculations.

Atom	Core-states	Local channel	r_{loc} (a.u.)	r_{nonloc} (a.u.)	r_{aug} (a.u.)	pseudopotential projectors	PAW projectors
H		p	0.8	0.8	0.6	2x2s	2x2s
O	1s	d	1.3	1.3	0.9	2x2s, 2x2p	2x2s, 2x2p
Na	1s	d	1.3	1.3	1.0	1x2s, 2x2p, 1x3s	1x2s, 2x2p, 1x3s
Si	1s, 2s,2p	d	1.8	1.8	1.3	2x3s, 2x3p	2x3s, 2x3p, 2x3d
Mg	1s, 2s	d	1.6	2.0	1.4	2x3s,1x2p, 2x3p	2x3s, 1x2p, 2x3p, 2x3d
Al	1s, 2s,2p	d	2.0	2.0	1.4	2x3s, 2x3p	2x3s, 2x3p, 2x3d
Pseudopotentials used for calculations on reference crystalline systems (see below)							
B	1s	d	1.4	1.4	1.0	2x2s, 2x2p	2x2s, 2x2p
Ca	1s	f	1.6	2.0	1.4	1x3s, 2x3p, 1x4s	1x3s, 2x3p, 1x4s
P	1s, 2s, 2p	d	1.8	1.8	1.3	2x3s, 2x3p	2x3s, 2x3p,2x3d
K	1s, 2s, 2p	d	1.8	1.8	1.6	1x3s, 2x3p, 2x4s	1x3s, 2x3p, 2x4s
Ge	1s, 2s, 2p, 3s, 3p, 3d	d	2.3	2.3	1.5	2x4s, 2x4p	2x4s, 2x4p
Y	1s, 2s, 2p, 3s, 3p, 3d	f	2.0	2.0	2.0	1x4s, 2x4p, 2x4d, 1x5s	1x4s, 2x4p, 2x4d, 1x5s

Where r_{loc} is the pseudisation radius for the local component of the pseudopotential, r_{nonloc} is the pseudisation radius for the non-local components of the pseudopotential, and r_{aug} is the pseudisation radius for the charge augmentation functions. The corresponding Materials Studio Castep on-the-fly strings used to generate these potentials are:

```
H 1|0.8|3.675|7.35|11.025|10UU(qc=6.4)[]
O 2|1.3|16.537|18.375|20.212|20UU:21UU(qc=7.5)[]
Na 2|1.3|1.3|1|11.8|13.6|15.3|20U=-2.07:30U=-0.105:21U=-1.06U=+0.25[]
Mg 2|1.6|2|1.4|6|7|8|30NH:21U:31UU:32LGG(qc=4.5)[]
Al 2|2|3.675|5.512|7.717|30UU:31UU:32LGG[]
Si 2|1.8|3.675|5.512|7.35|30UU:31UU:32LGG[]
B 2|1.4|9.187|11.025|13.965|20UU:21UU(qc=5.5)[]
K 2|1.8|1.8|1.6|11|14.7|16.7|30U:40UU:31UU(qc=5.5)[]
Ge 2|2.3|2.3|1.5|4.4|6|9|40U=-0.44U=+0.25:41U=-0.15U=+0.25[]"
Y 3|2|2|2|8.5|10|11.1|40U:50U:41UU:42UU[]
Ca 3|1.6|2.0|1.4|7|9|10|30U:40U:31:32U=+0@+0.12U=+1.0@+0.12
```

The pseudopotential of Ca used the correction described by Profeta *et al.*[1]

Table S2. Calculated shieldings (σ_{iso}) and experimental chemical shifts (δ_{iso}) of reference systems of known crystal structure.

Nucleus	Compond, formula	Site #	Experimental shift (ppm)	Reference	Calculated shielding (ppm)
^{1}H	Brucite $Mg(OH)_2$	1	0	2	30.8
	diaspore AlO(OH)	1	9.2	This work	19.8
	Boehmite AlO(OH)	1	7.2	This work	22.2
	Talc	1	0.7	3	30.6
	Pyrophyllite	1	2.2	3	28.2
	KH_2PO_4	1	14.9	4	12.2
^{29}Si	α-quartz SiO_2	1	-107.4	5	429.6
	Cristoballite SiO_2	1	-108.5	5	430.9
	albite $NaAlSi_3O_8$	3	-105	6	428.0
		2	-97		419.0
		1	-93		414.4
	datolite $CaBSiO_4(OH)$	1	-83	5	404.4
	danburite $CaB_2Si_2O_8$	1	-89	5	410.1
	Pyrophyllite $Si_4Al_2O_{10}(OH)_2$	1	-94	6	416.7
	Talc $Si_4Mg_3O_{10}(OH)_2$	1	-97	6	420.0
	Na_2SiO_3	1	-76.8	5	396.9
	α-$Na_2Si_2O_5$	1	-93.6	7	416.5
	β-$Na_2Si_2O_5$	1	-85.6	7	406.5
		2	-87.5		408.0
	δ-$Na_2Si_2O_5$	1	-90.6	8	411.7
		2	-90.2		411.2
^{27}Al	Berlinite $AlPO_4$	1	42.9	9	512
	$YAlO_3$	1	10.7	10	545.31
	$Y_3Al_5O_{12}$	1	77.5	10	480.04
		2	2.1		553.33
	Sillimanite Al_2SiO_5	1	63.9	11	491.72
		2	4.7		549.07
	$Al_2Ge_2O_7$	1	36	11	516.15
	Andalusite Al_2SiO_5	1	35	12	518.21
		2	10		543.34
	Low albite $NaAlSi_3O_8$	1	62.7	13	486.69
	Albite $NaAlSi_3O_8$	1	63	13	486.7

Calculations of shieldings for crystalline model systems of known structure and experimental shifts are used to accurately calculate the isotropic ^{29}Si chemical shifts (δ_{iso}) from calculated ^{29}Si shieldings (σ_{iso}). This procedure compensates for possible systematic errors of the DFT calculations. All calculations were conducted on structures previously optimized with fixed unit cell parameters. The series of compounds listed in Table S2 led to the following relationships: $\delta_{iso}(ppm) = -0.793*\sigma_{iso} + 24.71$ for ^{1}H ; $\delta_{iso}(ppm) = -0.920*\sigma_{iso} + 288.45$ for ^{29}Si ; and $\delta_{iso}(ppm) = -0.977*\sigma_{iso} + 541.86$ for ^{27}Al.

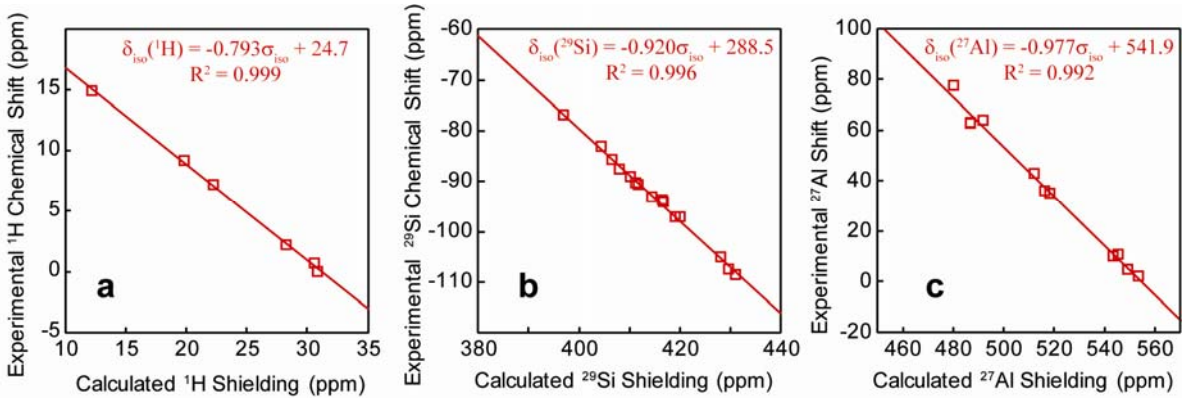

Figure S1. Correlation plots between experimental isotropic chemical shifts and isotropic shieldings calculated by DFT for the series of reference crystals of known structures listed in Table S2. (a), (b) and (c) correspond to ^{1}H, ^{29}Si, and ^{27}Al NMR data, respectively.

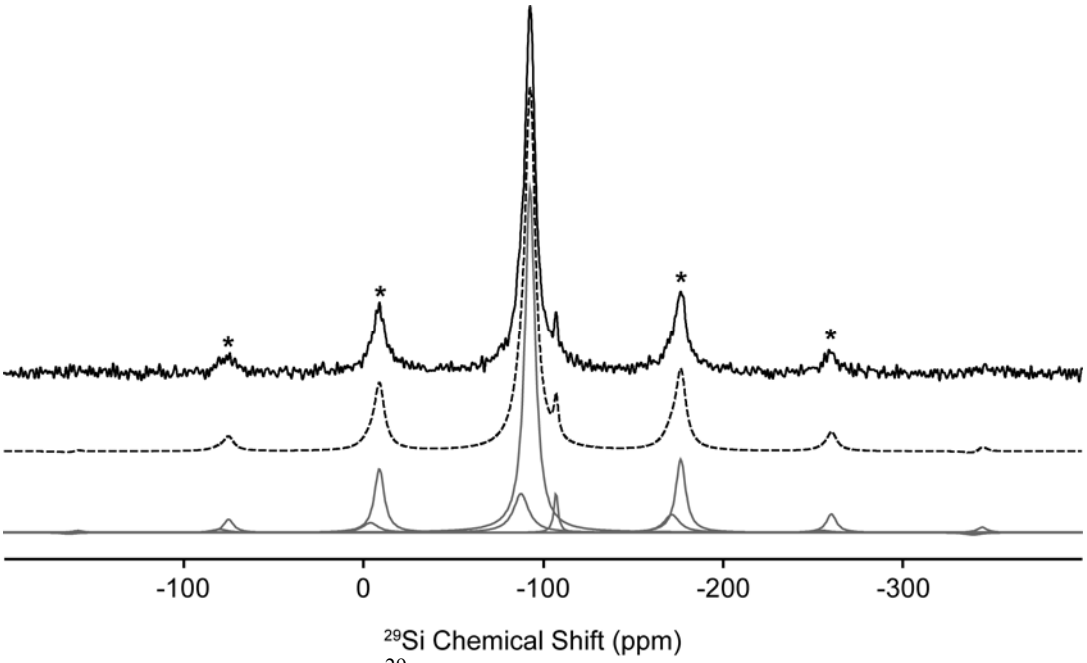

Figure S2. Solid-state NMR ^{29}Si echo-MAS spectrum of natural Na-Montmorillonite (same as in Figure 1c), collected at 8.8 T, 5 kHz MAS, using a short recycling delay of 200 ms (which considerably reduces the intensity of the slowly-relaxing quartz signal at -107 ppm). Spinning sidebands due to the effect of Fe^{3+} are marked with asterisks. The Q^3(1Al) contribution is confirmed in both the isotropic region and the sidebands.

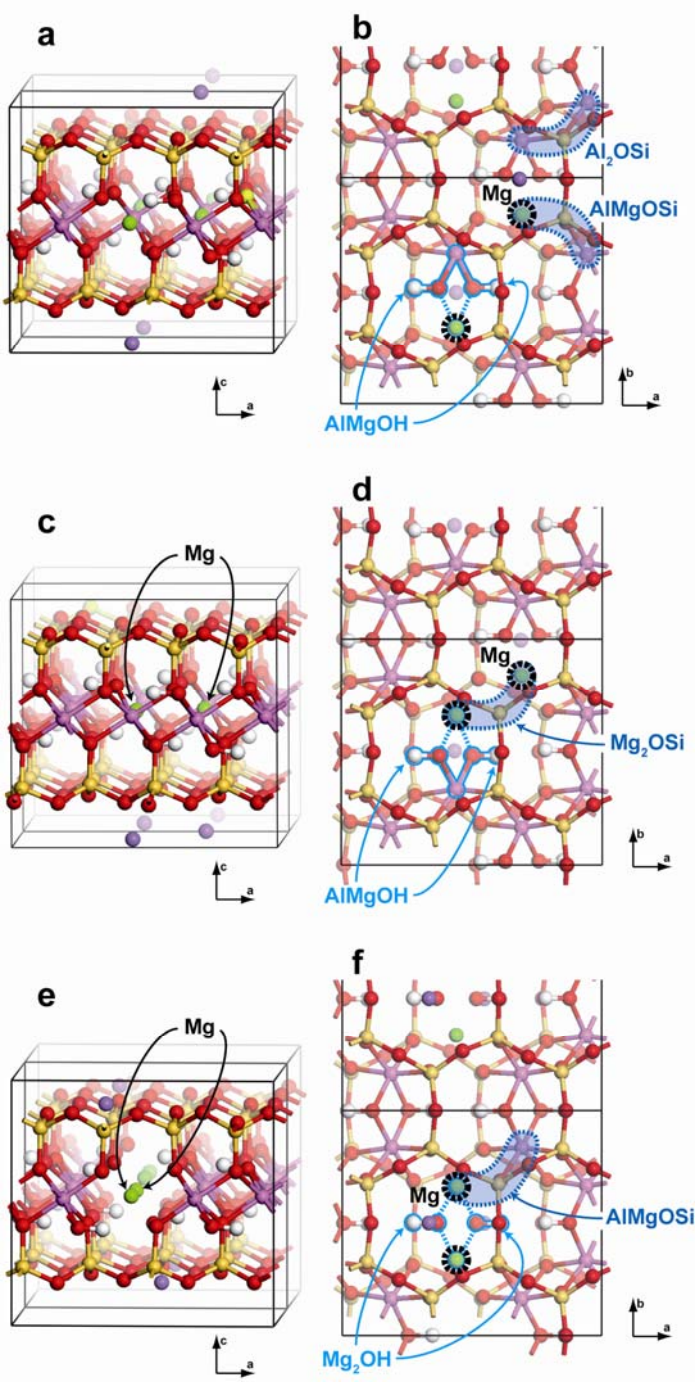

Figure S3. DFT-optimized models of Montmorillonite of composition $Na_2(Al^{(VI)}{}_6\mathbf{Mg_2})(Si_{16})O_{40}(OH)_8$, *i.e.* with two Mg atoms in the octahedral layer. In (a) Mg atoms occupy non-adjacent sites, whereas they occupy adjacent octahedral sites forming either (b) Mg_2OSi or (c) Mg_2OH moieties.

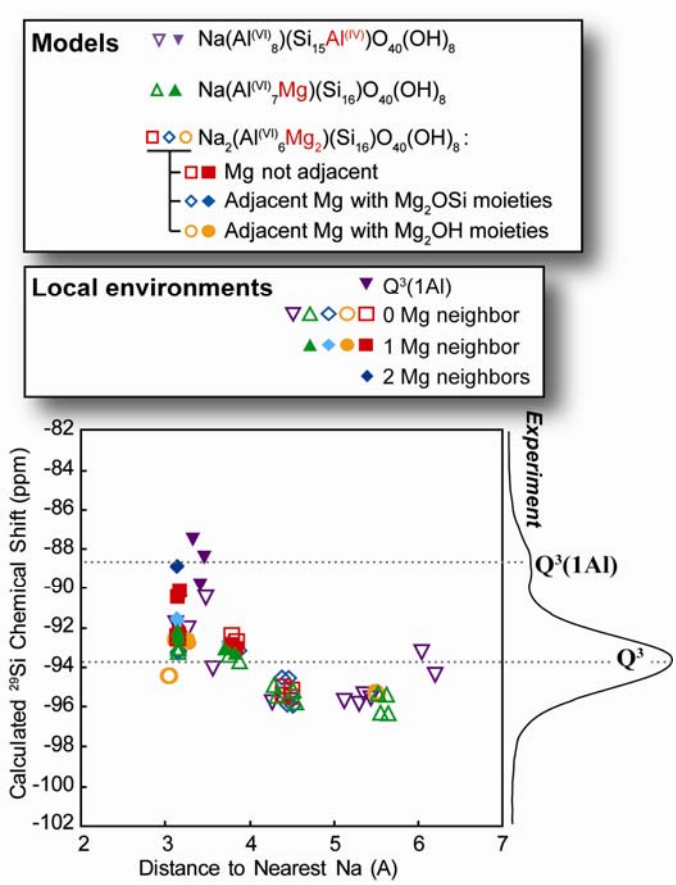

Figure S4. Plot of calculated ^{29}Si chemical shifts as a function of the distance to the nearest Na^+ cation, using all Montmorillonite models shown in Figure 5 and Supporting Information, Figure S3. Symbol types and colour tones refer to different models, while open or filled symbols and variations of colour tones point to distinct types of local environments. There appears to be an effect of the Si-Na distance on the calculated ^{29}Si chemical shifts, especially between ca. 3.5 and 6 Å.

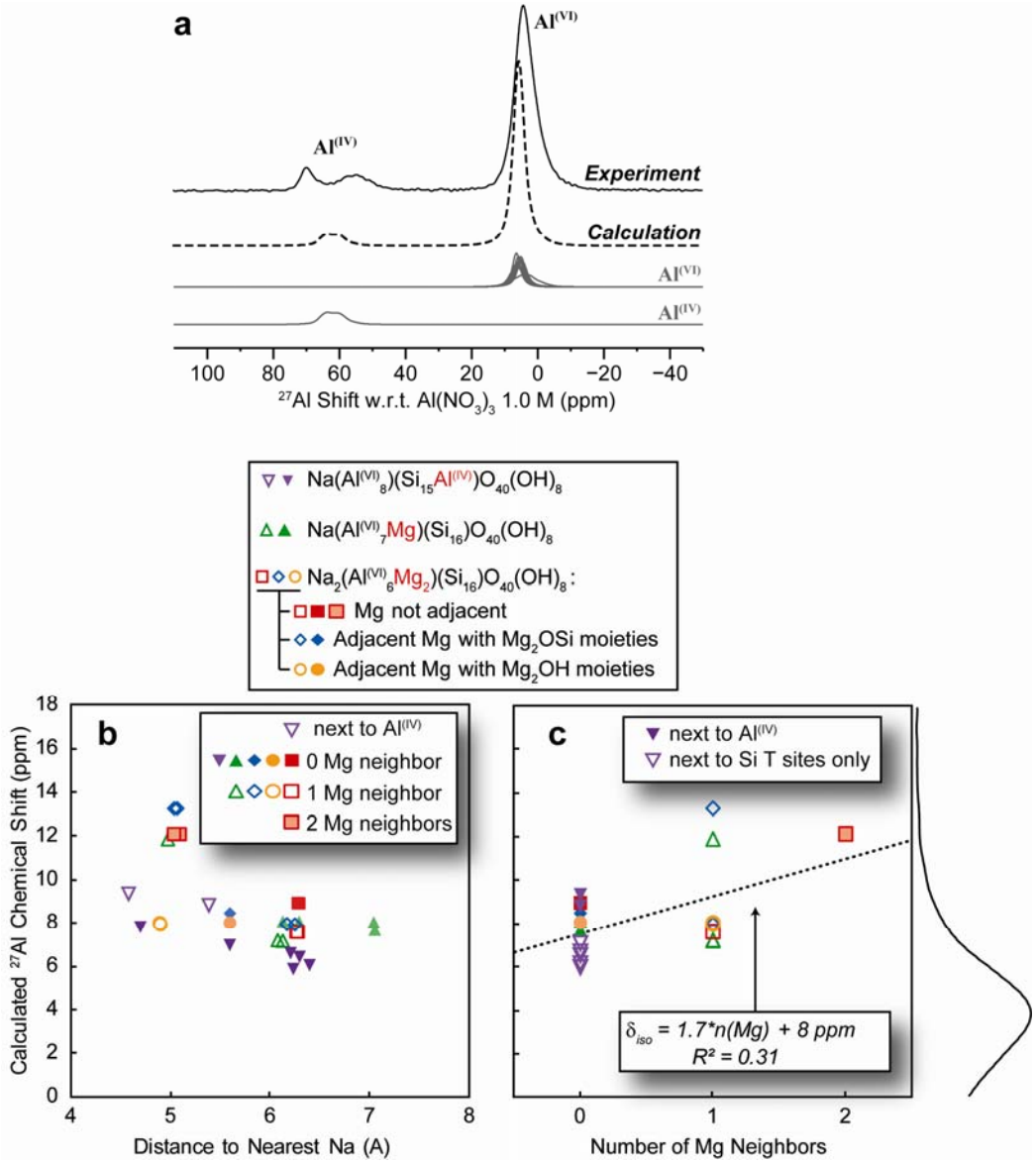

Figure S5. (a) Simulated ^{27}Al NMR spectrum (dashed line) obtained from DFT calculations of NMR parameters, using the structural model of composition $Na(Al^{(VI)}_8)(Si_{15}\mathbf{Al^{(IV)}})O_{40}(OH)_8$ (Figure 4a). The ^{27}Al MAS spectrum of Na-MMT (same as in Figure 2a) is shown on top for comparison (black solid line). Individual contributions from each site of the model to the calculated spectra are shown in grey lines. Arbitrary Lorentzian broadenings of 500 Hz were applied to each individual contribution. (b, c) Isotropic ^{27}Al chemical shifts calculated from DFT models shown in Figure 5 and Supporting information, Figure S3, and reported as functions of (b) the distance to the nearest Na atom, and (c) the number of Mg neighbors. Both parameters seem to contribute to some extent to the ^{27}Al shifts. We note that the model associated with yellow "○" is not representative of the actual material (absence of contribution from Mg_2OH moieties in ^{1}H NMR).

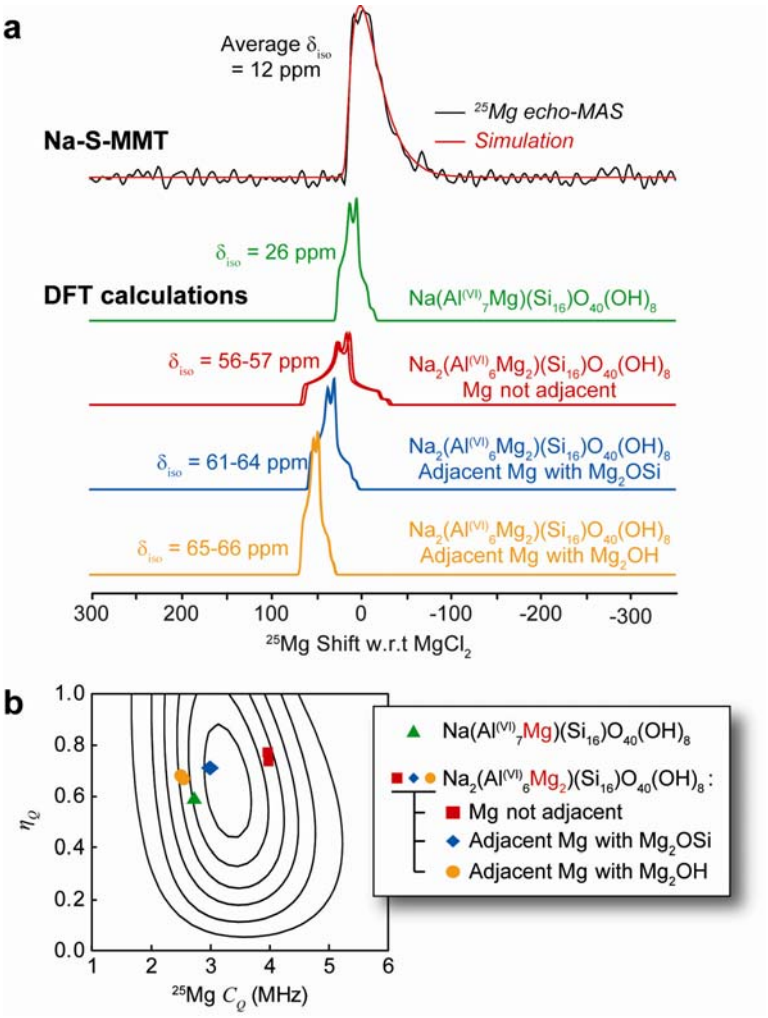

Figure S6. (a) ^{25}Mg MAS NMR spectrum of Na-S-MMT (in black, same as in Figure 3c) and corresponding simulation (in red) using the distribution of quadrupolar coupling parameters (C_Q, η_Q) plotted as contour levels in (b). The spectra represented in green, red, blue, and yellow in (a) correspond to the individual contributions calculated by DFT for the different Mg-containing models described above. The corresponding calculated quadrupolar coupling parameters are reported as symbols on top of the experimental distribution of quadrupolar coupling parameters in (b).

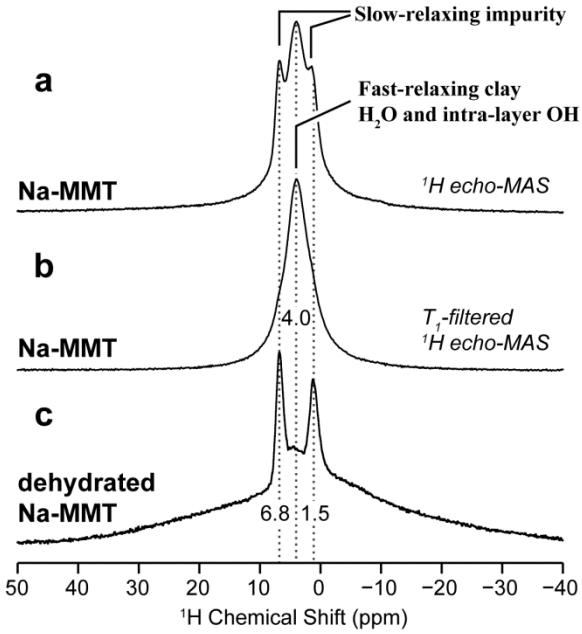

Figure S7. Solid-state ^{1}H echo-MAS NMR experiments performed on (a, b) natural montmorillonite (Na-MMT) and (c) dehydrated Na-MMT, at (a, b) 19.9 T and (c) 17.6 T, respectively, with a spinning frequency of 64 kHz. (a) Spectrum collected with a recycling delay of 10s. The contribution from the central peak at 4 ppm is underestimated due to its fast relaxation during the echo (two rotor periods). (b) Spectrum collected with a recycle delay of 0.1s and a large number of dummy scans to saturate the slow-relaxing components. (c) Spectrum collected with a recycling delay of 10s. The broad signal at the base is essentially due to rotor and probe background signals, which are not eliminated by the short echoes required to detect the fast relaxing clay signal.

Calculations of clay composition based on quantitative NMR data.

The composition of the tetrahedral layer may be calculated on the basis of ^{29}Si NMR data, assuming that the $Al^{(IV)}$ atoms are completely isolated from each other in the tetrahedral layer. This is a reasonable hypothesis given the low amount of four-coordinated Al in the material and following the Lowenstein rule, which predicts the avoidance of $Al^{(IV)}$-O-$Al^{(IV)}$ moieties and should at least partially apply in these materials.[14] We used the following formula:

$$(\mathrm{Si/Al^{(IV)}})_{\mathrm{NMR}} = \left(\sum_{n=0}^{3} I[Q^3(n\mathrm{Al})]\right) / \left(\sum_{n=0}^{3} (n/3) I[Q^3(n\mathrm{Al})]\right)$$

this yields a Si/Al ratio of 40 in the tetrahedral layer, corresponding to the composition ($Si_{7.80}Al_{0.20}$), calculated as:

$$n\left[\mathrm{Al}^{(IV)}\right] = \frac{n\left(\mathrm{Si} + \mathrm{Al}^{(\mathrm{IV})}\right)}{1 + \mathrm{Si/Al}^{(\mathrm{IV})}}$$

with $n\left(\mathrm{Si} + \mathrm{Al}^{(\mathrm{IV})}\right) = 8$, based on the theoretical composition of dioctahedral clays. The $Al^{(VI)}/Al^{(IV)}$ ratio is then used to derive the numbers of $Al^{(VI)}$, Mg, and inter-layer Na atoms.

Alternatively, the Mg and Al amounts in the octahedral layer may be obtained more directly from the relative amounts of AlMgOH and Al_2OH moieties using the expression:

$$n(\mathrm{Mg}) = \frac{n(\mathrm{OH})}{2\left(\frac{n(\mathrm{Al_2OH})}{n(\mathrm{AlMgOH})} + 1\right)}$$

with n(OH) = 4 (based on the theoretical composition of dioctahedral clays), which integrates the absence of Mg_2OH moieties, as demonstrated by ^{1}H NMR. We note that this does not preclude the existence of adjacent Mg, since the formula still works if pairs of adjacent Mg atoms are present in the form of Mg_2OSi moieties, i.e. Mg atoms "connected" via an apical O. The numbers of $Al^{(IV)}$, Si, and inter-layer Na atoms are then derived using the measured $Al^{(VI)}/Al^{(IV)}$ ratio.

Trying to correct the ICP-EOS data to account for the amounts of Al and Si in the aluminosilicate impurity detected by NMR (*i.e.* 13% of total Al content, in the form of $Al^{(IV)}$ only, and 16% of the total Si content) is done as follows:

$$n\left[\mathrm{Al}^{(IV)}\right]_{\mathrm{MMT}} = n\left[\mathrm{Al}^{(IV)}\right]_{\mathrm{ICP-EOS}}\left(1 - \frac{n\left[\mathrm{Al}^{(IV)}\right]_{\mathrm{Impurity}}}{n[\mathrm{Al}^{(IV)}]_{\mathrm{Total}}}\right)$$

and

$$n(\mathrm{Si})_{\mathrm{MMT}} = n(\mathrm{Si})_{\mathrm{ICP-EOS}}\left(1 - \frac{n(\mathrm{Si})_{\mathrm{Impurity}}}{n(Si)_{\mathrm{Total}}}\right)$$

We obtain a corrected $[\mathrm{Si/Al}^{(\mathrm{IV})}]_{\mathrm{MMT}}$ ratio of 85, which is not very different from the original $(\mathrm{Si/Al}^{(\mathrm{IV})})_{\mathrm{ICP}}$ ratio and still far from the ratios (between 30 and 40) calculated from NMR data.

References of the Supporting Information Section.

1. M. Profeta, M. Benoit, F. Mauri and C. J. Pickard, *J. Am. Chem. Soc.*, 2004, **126**, 12628-12635.
2. P. J. Sideris, U. G. Nielsen, Z. H. Gan and C. P. Grey, *Science*, 2008, **321**, 113-117.
3. M. D. Alba, A. I. Becerro, M. A. Castro, A. C. Perdigon and J. M. Trillo, *J. Phys. Chem. B*, 2003, **107**, 3996-4001.
4. J. T. Rasmussen, M. Hohwy, H. J. Jakobsen and N. C. Nielsen, *Chem. Phys. Lett.*, 1999, **314**, 239-245.
5. J. F. Stebbins, in *Handbook of Physical Constants*, ed. T. J. Ahrens, American Geophysical Union, Washington D.C., 1995, vol. 2.
6. K. J. D. Mackenzie and M. E. Smith, *multinuclear solid-state NMR of inorganic materials*, Pergamon Press, Oxford, 2002.
7. H. Koller, G. Engelhardt, A. P. M. Kentgens and J. Sauer, *J. Phys. Chem.*, 1994, **98**, 1544-1551.
8. L. Martel, S. Cadars, E. Véron, D. Massiot and M. Deschamps, *Solid State Nucl. Mag.*, 2012, **45–46**, 1-10.
9. D. Massiot, F. Fayon, B. Alonso, J. Trebosc and J. P. Amoureux, *J. Magn. Reson.*, 2003, **164**, 160-164.
10. P. Florian, M. Gervais, A. Douy, D. Massiot and J.-P. Coutures, *The Journal of Physical Chemistry B*, 2000, **105**, 379-391.
11. D. Massiot, *Journal of Magnetic Resonance, Series A*, 1996, **122**, 240-244.
12. L. B. Alemany, D. Massiot, B. L. Sherriff, M. E. Smith and F. Taulelle, *Chem. Phys. Lett.*, 1991, **177**, 301-306.
13. R. J. Kirkpatrick, R. A. Kinsey, K. A. Smith, D. M. Henderson and E. Oldfield, *Am. Mineral.*, 1985, **70**, 106-123.
14. J. Sanz and J. M. Serratosa, *J. Am. Chem. Soc.*, 1984, **106**, 4790-4793.